ICAS-88-5.5.1

VISCOUS/INVISCID INTERACTION PROCEDURE FOR HIGH-AMPLITUDE OSCILLATING AIRFOILS

W. Geißler
DFVLR Institute of Aeroelasticity, Göttingen, F. R. Germany

L. W. Carr
US Army Aeromechanics Laboratory, NASA-Ames Research Center,
Moffett Field, California, USA

T. Cebeci
Center for Aerodynamic Research, Cal. State University,
Long Beach, California, USA

Abstract

In a joint effort between the DFVLR, NASA-Ames and Cal. State University Long Beach, USA, a viscous/inviscid interaction procedure has been developed to calculate the unsteady viscous flow around airfoils operating under dynamic stall conditions. The inviscid part of this procedure is represented by a time-marching subsonic panel method which uses appropriate distributions of unsteady surface and wake singularities. Unsteady pressures as well as lift and moment distributions show good agreement with experimental data as long as viscous effects remain small. For increasing mean incidences and oscillation amplitudes, however, unsteady viscous effects become important. Experiments by McCroskey, Carr et al. have shown that reversed flow areas develop in time over parts of the airfoil upper surface, i.e. separation is delayed by unsteady motion. The flow may even be reversed and boundary layer-like over almost the entire upper surface until a strong (dynamic stall) vortex ultimately develops at the leading edge which changes the flow characteristics completely.

An unsteady boundary layer procedure has been coupled with the panel method. This strong coupling allows a detailed investigation of the complicated unsteady viscous flow phenomena involved. The inverse boundary layer method is an unsteady extension of the method for steady flow around airfoils at high incidences developed by Cebeci et al. using the Hilbert integral formulation. A laminar or turbulent boundary layer calculation can be performed using the two-region algebraic eddy viscosity concept by Cebeci/Smith in the turbulent case. The transition point and its development in time is prescribed in the present version of the method.

1. Introduction

A detailed understanding of unsteady viscous flow phenomena has been of increasing concern in recent years. Unsteady separation occurs on blades of helicopter rotors and wind energy converters as well as on turbomachinery cascades. This phenomenon, known as *dynamic stall*, may be the origin of dangerous stall flutter. On the other hand stall delay on wings in accelerated motion may successfully be used to increase the high maneuverability properties of combat aircraft. In the present study a few fundamental aspects of unsteady viscous flows around airfoils operating under dynamic stall conditions will be analytically investigated by means of a strong coupling procedure between an unsteady potential-theoretical and an inverse boundary layer code.

Extensive windtunnel tests on oscillating airfoils[1,2] have shown that the dynamic stall phenomenon may occur in different degrees of severity. Depending on profile geometry, incidence variation, frequency of oscillation, Reynolds and Mach number, one can distinguish between either light or deep dynamic stall conditions, with all variations in between. Experiments have shown further that, in the case of light dynamic stall, the flow may remain boundary layer-like about the airfoil although extended areas of reversed flow are developing over the airfoil's upper surface. The present study concentrates on the light dynamic stall cases where the assumption still holds that viscosity is restricted to a relatively thin region adjacent to the airfoil surface. In cases of deep dynamic stall, however, the flow breaks off the surface completely and concentrated vortices may develop. These cases are not within the scope of the present study.

It has been pointed out[3] that coupling between an unsteady panel method and a boundary layer code *in the direct mode* may lead to a breakdown of the numerical calculation due to unsteady separation. No simple separation criterion was found in these cases. But by integrating along the vectors of the maximum reversed flow velocities inside the boundary layer, typical envelopes were observed in the x,t-domain ($x \triangleq$ surface coordinate, $t \triangleq$ time) which were interpreted as the time-dependent locations of separation.[3] In a number of recent publications,[4] singularity has been completely avoided in the steady case by means of a strong viscous/inviscid coupling procedure. Airfoil incidences even close to stall could then be treated successfully. In the viscous part of the procedure[4] the Hilbert integral formulation was used to modify the external velocity distribution $U(x)$ within regions of strong viscous interaction. Here, $U(x)$ was part of the iterative solution procedure and allowed to adjust to the boundary layer displacement effect. Lift as well as drag coefficients obtained by this method show good agreement with corresponding experimental data.

A similar local strong interaction procedure with quasi-simultaneous viscous/inviscid coupling has been described recently,[5] with emphasis being placed on the interactions between the trailing edge and the near wake.

The present paper describes a coupling procedure between an unsteady subsonic panel method and a finite difference code to calculate the unsteady two-dimensional laminar/turbulent boundary layer equations around oscillating airfoils. Here the main features described in Refs. [4] and [6] for steady flows are followed also in the unsteady case. The Hilbert integral concept is used in regions of strong viscous interaction with several succes-

sive sweeps through the boundary layer per time step. A few global iterations in combination with the inviscid method are necessary in addition to get a final converged solution for a complete cycle of oscillation. For turbulent flows the two-region algebraic eddy viscosity concept by Cebeci and Smith is used on a quasi-steady basis. The location of transition from laminar to turbulent flow is prescribed simply in space and time. Two further problems have to be taken into consideration for unsteady flow problems:

1. The region of integration of the boundary layer equations is moving in time due to the movement of the front stagnation point.
2. Due to the explicit solution procedure of the present method in the x- and t-domain, a stability-bound (CFL condition) has to be taken into account.

The first problem is solved by a new transformation procedure using a time-variable boundary layer grid. The second problem is controlled simply by restricting mesh sizes in the x,t-domain. A further problem is the treatment of the unsteady wake. The effect of wake circulation is fully accounted for in the inviscid part of the problem via the unsteady Kutta condition. The displacement effect of the wake, however, is simply accounted for by an analytical formula representing a sink distribution with exponential decay along the wake center line. In the following, the main features of the method will first be outlined to some detail. Then results will be presented to show the flow characteristics inside the unsteady boundary layer. Overall lift, moment and drag coefficients will be presented and compared with experimental data.

2. Unsteady inviscid method

The inviscid flow about an oscillating airfoil is calculated by means of a subsonic panel method, which represents the airfoil surface and unsteady wake by corresponding source/sink and vorticity distributions.[7] For the incidence variation

$$\alpha(T) = \alpha_0 + \alpha_1 \sin \omega^* T \tag{1}$$

with $T = \dfrac{t \cdot U_\infty}{c}$ (dimensionless time),

and $\omega^* = \dfrac{\omega \cdot c}{U_\infty}$ (reduced frequency),

($U_\infty \triangleq$ undisturbed velocity, $c \triangleq$ airfoil chord),

a time-dependent circulation $\Gamma_p(T)$ develops around the airfoil. The change of "bound" circulation in time

$$\frac{\partial \Gamma_p}{\partial T}\, dT = \frac{\partial \gamma_p}{\partial T}\, dT \cdot s_p = -\gamma_w \cdot ds_w \tag{2}$$

(with s_p as the total arc length of the profile surface) is shed into the wake in agreement with the vorticity transport equation and determines the vorticity loading γ_w of a wake element ds_w at a specific instant of time T. If time is increasing, an increasing number of vorticity-loaded wake elements is formed. These elements are assumed to move downstream with the undisturbed flow speed U_∞. It is further assumed that the wake geometry is simply represented by a straight line forming an incidence of $\alpha_0/2$ (half the steady mean incidence) with respect to the airfoil axis.

The time-dependent incidence of Eq. (1) defines a kinematic velocity $\vec{V}_{\text{kin}}(T)$ in points on the airfoil surface. With the sum of the kinematic velocity and the induced velocities of all sources/sinks: $\vec{v}_q$ and vortices (on profile and wake): $\vec{v}_\gamma$, the kinematic flow condition for each instant of time yields

$$\vec{\zeta}\,(\vec{V}_{\text{kin}} + \vec{v}_q + \vec{v}_\gamma) = 0\,. \tag{3}$$

In Eq. (3) $\vec{\zeta}$ is the unit normal vector (outside positive) in points on the airfoil surface. If all known quantities in Eq. (3) are shifted to the right-hand side:

$$\vec{\zeta} \cdot \vec{v}_q = -(\vec{\zeta}\,\vec{V}_{\text{kin}} + \vec{\zeta}\,\vec{v}_\gamma) \tag{4}$$

a Fredholm integral equation of the second kind is obtained for the unknown source strengths of $\vec{v}_q$ at time T. Due to the discretization of the airfoil surface and wake into panels, Eq. (4) can be represented by a linear system of equations where the left-hand (source) part forms a large time-independent quadratic matrix of $M \times M$ elements ($M \triangleq$ number of surface panels) which has to be inverted only once before starting the unsteady solution procedure. The constant vorticity strength $\gamma_p(T)$ in $\vec{v}_\gamma$ is also unknown at this step and is first set equal to unity. Its value is calculated in a further step by applying the Kutta condition at the trailing edge:

$$\lim_{s \to s_{TE}} (c_{p_u}(T) - c_{p_\ell}(T)) = 0\,, \tag{5}$$

where s is the coordinate along the slope of the airfoil, c_{p_u} and c_{p_ℓ} are the trailing edge values of the instantaneous pressure coefficients on the upper and lower surface, respectively. From Eq. (5) a quadratic equation for $\gamma_p(T)$ can be formulated and solved explicitly.

Once all source and vortex strengths are known, the corresponding relative velocities (relative to the airfoil surface)

$$\vec{w} = \vec{V}_{\text{kin}} + \vec{v}_q + \vec{v}_\gamma \tag{6}$$

together with the time derivative of the potential are inserted into the unsteady Bernoulli equation:

$$c_p(\overline{T}) = -2\,\frac{\omega^*}{2\pi}\,\frac{\partial \Phi}{\partial \overline{T}} + \vec{V}_{\text{kin}} \cdot \vec{V}_{\text{kin}} + \vec{w} \cdot \vec{w} \tag{7}$$

with $\overline{T} = T\,\dfrac{\omega^*}{2\pi}\,, \qquad 0 \le \overline{T} \le 1\,.$ (8)

Integrating along the airfoil surface, the corresponding time-dependent lift, drag and moment coefficients ($c_L(\overline{T})$, $c_M(\overline{T})$, $c_D(\overline{T})$) are obtained.

3. Unsteady boundary layer method

It has already been pointed out that, for an oscillating airfoil, the front stagnation point is moving in time. However, problems arise if the boundary layer calculation has to start at the instantaneous positions of the stagnation points which are assumed to be known from the inviscid calculation of Chapter 2.

In Ref. [3] problems are avoided by calculating the boundary layer within the stagnation point region on a quasi-steady basis and then continue with the unsteady calculation further downstream. This procedure has the disadvantage that, for high-amplitude oscillations, the stagnation point moves several percent of the airfoil chord along the leading edge and unsteady effects inside the

boundary layer are assumed to be no longer negligible within this region. In a different approach,[8] the boundary layer surface coordinate was attached rigidly to the moving stagnation point. In this case difficulties occur at the airfoil's trailing edge which is not a point of the moving system. The retro-transformation and interpretation of the results in surface-fixed coordinates is not straightforward. The unsteady loading edge flow was recently investigated in detail.[9]

In the present approach the coordinate system for the boundary layer calculation is attached to the stagnation point (***Fig. 1***) as well as to the trailing edge of the airfoil. The grid is therefore allowed to stretch and shrink with time.

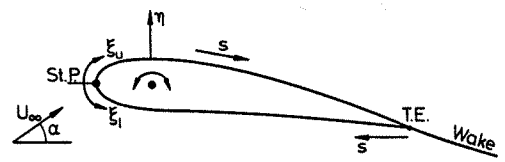

Figure 1: **Coordinate system for oscillating airfoil**

Fig. 2 shows the coordinate mesh in the physical x,t-plane and in the computational ξ,τ-plane. The lines ξ = constant are obtained by subdividing the surface slope between the stagnation point and the trailing edge into equal numbers of grid points for each instant of time.

The transformation rule is given by

$$\begin{aligned} \xi &= \xi(x,t)\,, && \text{surface coordinate, Fig. 1} \\ \eta &= \eta(y)\,, && \text{normal coordinate, Fig. 1} \\ \tau &= \tau(t)\,, && \text{time,} \end{aligned} \tag{9}$$

where the metric coefficients

$$\frac{\partial \xi}{\partial t} \neq 0 \qquad \text{and} \qquad \frac{\partial \xi}{\partial x} \neq 1 \tag{10}$$

now have to be taken into account.

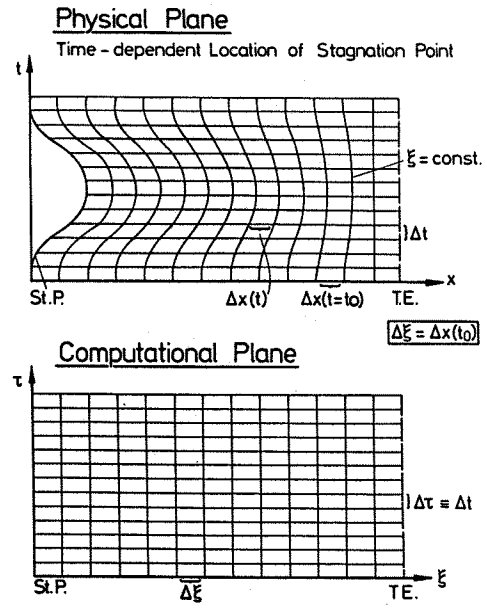

Figure 2: **Coordinate transformation**

3.1 Boundary layer equations in moving coordinates

With the transformation conditions (Eq. (9) and Fig. 2) the unsteady 2-d boundary layer equations can be expressed in moving coordinates:

Continuity equation

$$\frac{\partial}{\partial \xi}\left[u\left(\frac{\partial \xi}{\partial x}\right)^2\right] + \frac{\partial}{\partial \eta}\left(v\,\frac{\partial \xi}{\partial x}\right) = 0\,. \tag{11}$$

Momentum equation

$$\begin{aligned} &\frac{\partial u}{\partial \tau}\cdot\frac{\partial \xi}{\partial x} + u\,\frac{\partial u}{\partial \xi}\left(\frac{\partial \xi}{\partial x}\right)^2 + \frac{\partial}{\partial \xi}\left(u\,\frac{\partial \xi}{\partial t}\cdot\frac{\partial \xi}{\partial x}\right) + v\,\frac{\partial u}{\partial \eta}\cdot\frac{\partial \xi}{\partial x} = \\ &\frac{\partial U}{\partial \tau}\cdot\frac{\partial \xi}{\partial x} + U\,\frac{\partial U}{\partial \xi}\left(\frac{\partial \xi}{\partial x}\right)^2 + \frac{\partial}{\partial \xi}\left(U\,\frac{\partial \xi}{\partial t}\cdot\frac{\partial \xi}{\partial x}\right) + \\ &+ \frac{1}{Re}\left(\frac{\partial \xi}{\partial x}\right)\frac{\partial}{\partial \eta}\left(b\,\frac{\partial u}{\partial \eta}\right) \end{aligned} \tag{12}$$

with the boundary conditions

$$\begin{aligned} \eta &= 0 \;: u = v = 0\,, \\ \eta &\to \infty \;: u = U\,. \end{aligned}$$

In Eqs. (11) and (12) all lengths are in terms of the airfoil chord c and all velocities are in terms of U_∞. The term b in Eq. (12) includes the turbulent eddy viscosity ν_t (see Section 3.4) with

$$b = 1 + \frac{\nu_t}{\nu} \qquad (\nu \triangleq \text{kinematic viscosity})\,. \tag{13}$$

System (11), (12) is rendered independent from the Reynolds number by the transformation

$$\begin{aligned} \bar{\eta} &= \eta\sqrt{Re}\,, \\ \bar{v} &= v\sqrt{Re}\,. \end{aligned} \tag{14}$$

Introducing a stream function

$$\psi = \bar{\psi}\,\frac{U_\infty c}{\sqrt{Re}} \tag{15}$$

the continuity equation (11) is not always automatically fulfilled in the moving system. A term

$$\frac{\partial}{\partial \xi}\left(\frac{\partial \xi}{\partial x}\right)^2 \tag{16}$$

remains, which is only zero if $(\partial\xi/\partial x)_{t,y}$ = constant. The latter condition can be achieved with an equally spaced mesh in both x,y,t- and ξ,η,τ-domains (Fig. 2).

With Eq. (15) the momentum equation (12) yields

$$\begin{aligned} &\frac{\partial \bar{\psi}'}{\partial \tau} + \bar{\psi}'\,\frac{\partial \bar{\psi}'}{\partial \xi}\left(\frac{\partial \xi}{\partial x}\right) + \frac{\partial}{\partial \xi}\left(\bar{\psi}'\,\frac{\partial \xi}{\partial t}\right) - \frac{\partial \bar{\psi}}{\partial \xi}\,g = \\ &\frac{\partial U}{\partial \tau} + U\,\frac{\partial U}{\partial \xi}\left(\frac{\partial \xi}{\partial x}\right) + \frac{\partial}{\partial \xi}\left(U\,\frac{\partial \xi}{\partial t}\right) + (b\cdot g)'\,, \end{aligned} \tag{17}$$

where the primemark denotes differentiation with respect to $\bar{\eta}$. The boundary conditions for Eq. (17) are

$$\begin{aligned} \bar{\eta} &= 0 \;: \bar{\psi} = \bar{\psi}' = 0\,, \\ \bar{\eta} &\to \infty \;: \bar{\psi}' = U\,. \end{aligned} \tag{18}$$

In Eq. (17) the underlined terms refer to the moving coordinate system. With the additional defining equations

$$\overline{\psi}' = u \tag{19}$$

and

$$u' = g = \overline{\psi}'' \tag{20}$$

the system (17)−(20) forms the final set of first-order equations which has to be solved by numerical methods.

3.2 Eddy viscosity, transition

In regions of turbulent boundary layer flow the turbulent viscosity ν_t in Eq. (13) requires a turbulence model. Here the algebraic eddy viscosity concept by Cebeci and Smith[10] is used. The term ν_t is expressed by two different formulas representing the inner and outer region inside the boundary layer. In transformed variables the inner part within the region $0 \le \overline{\eta} \le \overline{\eta}_c$ yields

$$\left(\frac{\nu_t}{\nu}\right)_i = 0.16\sqrt{Re}\,\overline{\psi}''\overline{\eta}^2\left(1 - e^{-\overline{\eta}/A}\right)^2 \gamma_{tr} , \tag{21}$$

with

$$A = \frac{26}{\sqrt[4]{Re}\,\sqrt{\overline{\psi}''_{\max}}}$$

($\overline{\psi}''_{\max} \triangleq$ maximum value inside the boundary layer)

and the outer part is represented by

$$\left(\frac{\nu_t}{\nu}\right)_o = 0.0168\sqrt{Re}\,(U\eta_e - \overline{\psi}_e)\gamma_{tr} . \tag{22}$$

Both Eqs. (21) and (22) coincide at $\overline{\eta}_c$ using the condition of continuity of the eddy viscosity terms.

The term γ_{tr} in Eqs. (21) and (22) represents an intermittency factor which accounts for the transitional region between laminar and turbulent flow:

$$\gamma_{tr} = 1 - e^{-G\int_{x_{tr}}^{x}\frac{dx}{U}} \tag{23}$$

with

$$G = \frac{1}{1200}\cdot\frac{U^3 Re^2}{Re_{x_{tr}}^{1.34}} \tag{24}$$

and the transition Reynolds number

$$Re_{x_{tr}} = U \cdot x \cdot Re . \tag{25}$$

The coordinate x in Eqs. (23)−(25) is measured in the physical domain (Fig. 2) from the instantaneous position of the stagnation point.

In the present study transition has always been fixed two mesh points behind the stagnation point on the upper and lower surfaces of the airfoil. The consequence of this simplification is a rigid movement of the transition point with the stagnation point. Further intensive studies are necessary to improve the prediction of the instantaneous position of the transition point. In the steady case[4] it has been pointed out that, in cases of high incidence, the transition location has a very sensitive influence on the development of the boundary layer and on the final lift and drag coefficients.

3.3 Inverse formulation

If the system (17)−(20) is solved in the direct mode the external time-dependent velocity distribution $U(\xi, \overline{T}) \equiv \vec{w}$ (Eq.(6)) remains unchanged during the viscous solution procedure. This assumption is no longer valid if strong viscous/inviscid interaction is involved due to severe boundary layer displacement effects. In this case the external velocity distribution is modified by means of the Hilbert integral concept:

$$W(\xi, \overline{T}) = U(\xi, \overline{T}) + \delta U(\xi, \overline{T}) , \tag{26}$$

where $\delta U(\xi, \overline{T})$ is the influence of the boundary layer displacement effect upstream and downstream of ξ. In the transformed coordinate system, Eq. (26) becomes

$$\delta U(\xi, \overline{T}) = \frac{1}{\pi}\frac{\partial \xi}{\partial x}\int_{\xi_a}^{\xi_b}\frac{d}{d\xi'}(U\delta^*)\frac{d\xi}{\xi - \xi'} \tag{27}$$

($\xi \triangleq$ control point, $\xi' \triangleq$ inducing point).

In Eq. (27) ξ_a and ξ_b define the upstream and downstream limits of the interactive region. The term $\delta U(\xi, \overline{T})$ in Eq. (27) can be interpreted as the induced velocity of a continuous source distribution between ξ_a and ξ_b of strength $d/d\xi'\,(U\delta^*)$ with

$$\delta^* = \frac{1}{\sqrt{Re}}\left(\overline{\eta}_e - \frac{\overline{\psi}_e}{U}\right) \tag{28}$$

as the boundary layer displacement thickness ($\overline{\eta}_e$ and $\overline{\psi}_e$ are values at the outer edge of the boundary layer). Eq. (27) can be discretized as described in Ref. [11] by

$$W_i(\xi, \overline{T}) = U_i(\xi, \overline{T}) + \frac{\partial \xi}{\partial x}\sum_{j=1}^{n} c_{i,j}(U\delta^*)_j , \tag{29}$$

with $c_{i,j}$ representing geometric influence coefficients of the inducing elements j in control points i. Rearranging the unknowns in Eq. (29) on the right-hand side yields

$$W_i - \overline{c_{i,i}}(\overline{\eta}_e W_i - \overline{\psi}_e) = U_i + \frac{\partial \xi}{\partial x}\left\{\sum_{j=1}^{i-1} c_{i,j}(U\delta^*)_j + \sum_{j=i+1}^{n} c_{i,j}(U\delta^*)_j\right\} = g_i \tag{30}$$

with

$$\overline{c_{i,i}} = \frac{c_{i,i}}{\sqrt{Re}}\frac{\partial \xi}{\partial x} . \tag{31}$$

If the boundary layer equations are solved in the inverse mode, the external velocity component W in Eq. (30) is assumed to be an additional unknown and a fourth equation is necessary:

$$\frac{\partial W}{\partial \overline{\eta}} = 0 , \tag{32}$$

which will be discretized in the same way as Eqs. (17)−(20), modifying the external boundary condition (18) by

$$\overline{\psi}' = W . \tag{33}$$

Eq. (30) is then used as an additional condition for the unknown W.

3.4 Discretization and solution procedure

Fig. 3 shows the discretization molecule for the system of unsteady boundary layer equations (17)−(20) and (32). Eq. (17) is discretized at the midpoint of the box at $(j-1/2,\ i-1/2,\ n-1/2)$, whereas Eqs. (18), (19) and (32) are discretized at the side of the box at $(j-1/2,\ 2,\ 2)$. The

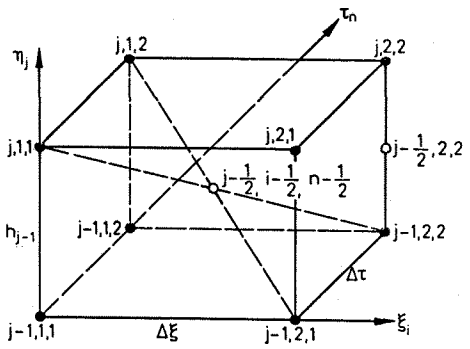

Figure 3: **Discretization molecule**

general features of the solution procedure are described in detail in Ref. [6] for steady 2-d inverse boundary layers as well as for unsteady 2-d boundary layers in the direct mode.

For application of Newton's method the nonlinear system of equations as well as the boundary conditions are first of all linearized:

$$\begin{aligned} \bar{\psi}_j &= \bar{\psi}_j^0 + \delta\bar{\psi}_j \ , \\ u_j &= u_j^0 + \delta u_j \ ; \qquad 0 \le j \le J \ , \\ g_j &= g_j^0 + \delta g_j \ , \\ W_j &= W_j^0 + \delta W_j \ , \end{aligned} \tag{34}$$

where the terms with superscript "0" denote appropriate starting values. Introducing Eqs. (34) into the discretized equations (17) – (20) and (32) yields for Eq. (19)

$$\delta\bar{\psi}_{j,2,2} - \delta\bar{\psi}_{j-1,2,2} - \frac{h_{j-1}}{2}\,(\delta u_{j,2,2} + \delta u_{j-1,2,2}) = (r_1)_j \tag{35}$$

with the boundary condition at the wall (Eq. (18)):

$$\delta\bar{\psi}_{1,2,2} = (r_1)_0 \equiv 0 \ . \tag{35a}$$

Eq. (17) is discretized and rearranged by

$$\begin{aligned} &(S1)_j\,\delta g_{j,2,2} + (S2)_j\,\delta g_{j-1,2,2} + (S3)_j\,\delta\bar{\psi}_{j,2,2} + \\ &+ (S4)_j\,\delta\bar{\psi}_{j-1,2,2} + (S5)_j\,\delta u_{j,2,2} + (S6)_j\,\delta u_{j-1,2,2} + \\ &+ (S7)_j\,\delta W_{j,2,2} + (S8)_j\,\delta W_{j-1,2,2} = (r_2)_j \end{aligned} \tag{36}$$

with the boundary condition at the wall

$$\delta u_{1,2,2} = (r_2)_0 \equiv 0 \ . \tag{36a}$$

The coefficients $(S1)_j - (S8)_j$, see ***Appendix***, are determined from the discretized momentum equation (17). Eq. (20) yields

$$\delta u_{j,2,2} - \delta u_{j-1,2,2} - \frac{h_{j-1}}{2}\,(\delta g_{j,2,2} + \delta g_{j-1,2,2}) = (r_3)_{j-1} \tag{37}$$

with the boundary condition, Eq. (30), at the outer edge of the boundary layer obtained from the inverse formulation

$$\gamma_1\,\delta\bar{\psi}_J + \gamma_2\,\delta W_J = (r_3)_J \ . \tag{37a}$$

In Eq. (37a), $\gamma_1 = 0$ and $\gamma_2 = 1$ represents the standard problem and

$$\gamma_1 = 1 \ ; \qquad \gamma_2 = \frac{1 - \bar{c}_{i,i}\,\eta_e}{\bar{c}_{i,i}} \tag{37b}$$

stands for the inverse formulation. Eq. (32) yields

$$\delta W_j - \delta W_{j-1} = W_{j-1} - W_j = (r_4)_{j-1} \tag{38}$$

with the boundary condition at the outer edge

$$\delta u_J - \delta W_J = (r_4)_J \ . \tag{38a}$$

The right-hand vectors $(r_1)_j - (r_4)_j$, see Appendix, are obtained again from the discretized versions of Eqs. (17) – (20) and (32).

With Eqs. (35) – (38) a linear system of equations is obtained for all grid points $0 \le j \le J$ through the boundary layer

$$\mathbf{A} \cdot \delta = \mathbf{r} \tag{39}$$

$$\text{with} \qquad \delta = \begin{bmatrix} \delta_0 \\ \delta_1 \\ \vdots \\ \delta_J \end{bmatrix} \ ; \qquad \mathbf{r} = \begin{bmatrix} r_0 \\ r_1 \\ \vdots \\ r_J \end{bmatrix} \tag{40}$$

and the tridiagonal matrix

$$\mathbf{A} = \begin{bmatrix} A_0 & C_0 & & 0 \\ B_1 & A_1 & C_1 & \\ & B_j & A_j & C_j \\ 0 & & B_J & A_J \end{bmatrix} . \tag{41}$$

The elements of matrix A represent 4×4 blocks corresponding to the four equations (35) – (38) to be solved with

$$A_j = \begin{bmatrix} 1 & -\frac{h_{j-1}}{2} & 0 & 0 \\ (S3)_j & (S5)_j & (S1)_j & (S7)_j \\ 0 & -1 & -\frac{h_j}{2} & 0 \\ 0 & 0 & 0 & -1 \end{bmatrix} ; \tag{42a}$$

$$1 \le j \le J-1$$

(42b)

$$B_j = \begin{bmatrix} -1 & -\frac{h_{j-1}}{2} & 0 & 0 \\ (S4)_j & (S6)_j & (S2)_j & (S8)_j \\ 0 & 0 & 0 & 0 \\ 0 & 0 & 0 & 0 \end{bmatrix} ; \qquad C_j = \begin{bmatrix} 0 & 0 & 0 & 0 \\ 0 & 0 & 0 & 0 \\ 0 & 1-\frac{h_j}{2} & 0 & \\ 0 & 0 & 0 & 1 \end{bmatrix} .$$

$$1 \le j \le J \qquad\qquad 0 \le j \le J-1$$

At the wall ($j = 0$) and at the outer edge of the boundary layer ($j = J$) the boundary conditions (Eqs. 35a, 36a and Eqs. 37a, 38a) enter the first two rows of matrix A_0 and the last two rows of matrix A_J, respectively:

$$A_0 = \begin{bmatrix} 1 & 0 & 0 & 0 \\ 0 & 1 & 0 & 0 \\ 0 & -1 & -\frac{h_j}{2} & 0 \\ 0 & 0 & 0 & -1 \end{bmatrix} ; \qquad A_J = \begin{bmatrix} 1 & -\frac{h_{J-1}}{2} & 0 & 0 \\ (S3)_J & (S5)_J & (S1)_J & (S7)_J \\ \gamma_1 & 0 & 0 & \gamma_2 \\ 0 & 1 & 0 & -1 \end{bmatrix} .$$

The solution vector δ_j and the right-hand vector r_j are represented by:

$$\delta_j = \begin{bmatrix} \delta\psi_{j,2,2} \\ \delta u_{j,2,2} \\ \delta g_{j,2,2} \\ \delta W_{j,2,2} \end{bmatrix} ; \quad r_j = \begin{bmatrix} (r_1)_j \\ (r_2)_j \\ (r_3)_j \\ (r_4)_j \end{bmatrix} . \qquad (44)$$

The block elimination method by Keller[12] and Cebeci and Bradshaw[13] is applied to solve the linear system (39). Only a few Newton iterations are necessary to obtain a final sufficiently converged solution of the linear system of equations. If the boundary layer calculation is carried out in the interactive mode, Eq. (30) has to be taken into account, with W as the unknown velocity. The interactive procedure can only be carried out iteratively. To start this iteration, $(U\delta^*)$-values (in Eq. (30)) from the previous time step are used and several sweeps through the interactive part of the boundary layer are made. It has been found that the number of sweeps can be limited with the present method to three in the unsteady part of the calculation. The interactive region can be extended further over the entire upper surface of the profile to take care of backflow regions in the vicinity of the airfoil's leading edge as well.

To start the unsteady calculation, appropriate initial values at a prescribed time line have to be determined. Here the procedure for interactive two-dimensional boundary layer flows[6] has been applied with the Flare approximation ($u\,\partial u/\partial x \equiv 0$ for $u < 0$) in regions of reversed flows. The $(U\delta^*)$-values for the first interactive sweep are now obtained from a direct 2-d steady solution of the boundary layer system up to the point of zero skin friction. The $(U\delta^*)$-values beyond the separation point are simply determined by extrapolation. In the steady case, about 13 to 15 iterations are necessary to obtain a sufficiently converged solution.

4. Viscous/inviscid coupling, global iteration

The converged source strengths in the Hilbert integral formulation of Eq. (27)

$$v_B(\xi, \overline{T}) = \frac{d}{d\xi}(U \cdot \delta^*) , \qquad (45)$$

i.e. the blowing or transpiration velocity, have to be taken into account in the inviscid panel method to modify the kinematic flow condition (Eq. 3)

$$\vec{\zeta}\,(\vec{V}_{kin} + \vec{v}_q + \vec{v}_\gamma) = v_B . \qquad (46)$$

The solution of Eq. (46) for the unknown source and vorticity strengths now includes the effects of boundary layer displacement along the airfoil surface. The blowing velocity also has to be taken into account in the Bernoulli equation in order to calculate the pressure distribution (Eq. 7)

$$c_p(\overline{T}) = -2\,\frac{\omega^*}{2\pi}\,\frac{\partial\phi}{\partial\overline{T}} + \vec{V}_{\text{kin}} \cdot \vec{V}_{\text{kin}} - (\vec{w} \cdot \vec{w} + v_B^2) \qquad (47)$$

and correspondingly in the Kutta condition (Eq. 5).

The latter condition is further modified by using control points which are located on the instantaneous displacement body surface instead of the airfoil surface itself.

After calculating the relative velocity distribution $\vec{w}$ (Eq. 6) now including the displacement effects of the boundary layer, a second global cycle starts with modified external velocities in the boundary layer calculation etc. Viscous as well as inviscid calculations are always extended over complete cycles of oscillation. For the start of the global viscous/inviscid iteration procedure, appropriate initial velocity distributions have to be determined. These initial values are obtained from the inviscid panel method by iterating over three complete cycles of oscillation. ***Fig. 4*** shows again the various steps of the global viscous/inviscid iteration procedure with the option of accelerating the convergence in step 3. This step however was not very effective and therefore not applied in the present calculations.

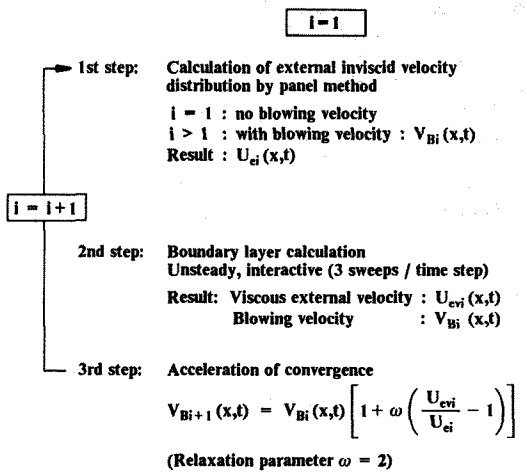

Figure 4: **Unsteady viscous/inviscid interaction procedure**

Fig. 5 displays the iteration history of the instantaneous lift coefficient for the NACA 0012 airfoil section at the maximum incidence of $\alpha(T) = 18°$ ($\omega^* = 0.4$, $Re = 2 \cdot 10^6$). The results from the first three cycles are derived from inviscid calculations. The first viscous cycle has been obtained with a Reynolds number 10 times larger than the nominal one ($2 \cdot 10^7$). Experience with the method has shown that, if the Reynolds number is not increased in this way, the lift after the first viscous cycle tends to overshoot to small values and requires additional

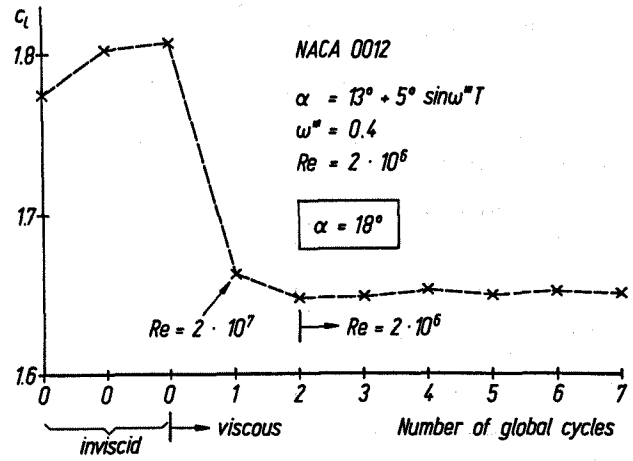

Figure 5: **Iteration history of the instantaneous lift**

iterations to approach a converged level. During the second and following global cycles the Reynolds number is reduced to the nominal value again. Fig. 5 shows that, even in the case of extreme incidence for the present coupling procedure, only three global cycles are necessary to obtain a satisfactory solution. For the results presented in the following sections, *three* global cycles were therefore assumed to be sufficient in all cases.

It has already been mentioned that the displacement effect of the wake is approximated by means of an analytical function:

$$q_w(s_w) = -[(U\delta^*)_u + (U\delta^*)_\ell]\, a \cdot e^{-9(s_w - s_{TE})} , \qquad (47)$$

where $q_w(s_w)$ is the strength of a distribution of sinks along the wake center line (s_w) with $(U\delta^*)_u$ and $(U\delta^*)_\ell$ obtained from the boundary layer calculation (indices u and ℓ refer to the upper and lower side at the trailing edge, respectively). If in Eq. (47) the parameter a is set equal to unity, the effect of the sink distribution along the wake on the pressures is presented in ***Fig. 6*** and compared with the case without sink distribution. Larger typical deviations can be observed in the trailing edge region. The lift and drag coefficients are slightly increased.

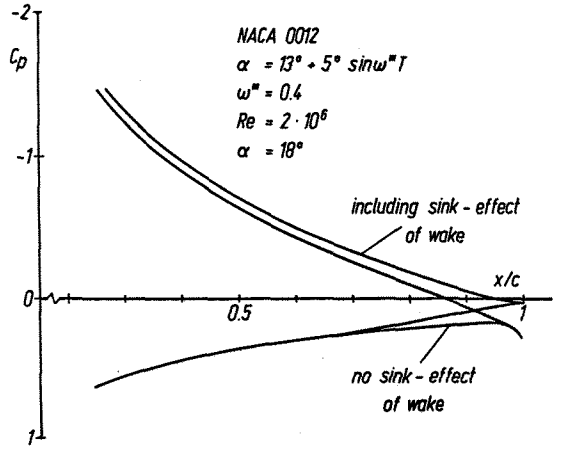

Figure 6: **Effect of wake sink distribution on trailing edge pressures**

Due to the fact that it is difficult to assume a reasonable value for the parameter a in Eq. (47), the present results are calculated without wake sink effects.

5. Results

The present method allows a reasonable number of parameters to be varied:

- airfoil geometry,
- incidence variation,
- reduced frequency,
- Reynolds number.

Some of these parameters will be investigated in the following sections. However, one important parameter, the Mach number, is missing. The incompressible treatment of the problem of airfoils oscillating at high incidences has its limitations. The incompressible minimum pressure coefficient $(c_{p_{min}})_{ic}$ may be related to the critical Mach number Ma^*:[14]

$$(c_{p_{min}})_{ic} = -\frac{2}{\kappa + 1} \frac{(1 - Ma_\infty^*)^{\frac{3}{2}}}{Ma_\infty^{*2}} ; \qquad (48)$$
$$(\kappa = 1.4) .$$

If the Mach number of the undisturbed flow is as low as 0.25, the limiting pressure coefficient is about -12, a value which may be reached for the NACA 0012 airfoil at incidences beyond $\alpha = 16°$. At $Ma = 0.3$ the limiting value is already reached at $c_p = -8$. If $c_{p_{min}}$ is exceeded, strong local supersonic regions may develop which change the pressure distributions and hence lift, moment and drag characteristics considerably. For comparisons with experimental data in Section 5.2, therefore, only data was selected[2] for which the assumption of incompressible flow still holds.

5.1 Details of unsteady viscous flow

One of the most important parameters for the oscillating airfoil problem is the frequency of oscillations expressed in dimensionless form by the reduced frequency ω^* (Eq. 1). Some emphasis will therefore be placed on a variation of ω^* and its effect on the various flow quantities involved. For the development of the time-dependent flow, the limiting values at $\omega^* = 0$, i.e. the quasi-steady limit, are of interest. The present computer code is therefore constructed such that the case $\omega^* = 0$ can be treated on the basis of a steady interacting boundary layer calculation coupled with the quasi-steady limit for the external inviscid flow. A complete incidence cycle can then be calculated as in the unsteady case. But for each incidence a larger number of sweeps (about 15) is necessary for a converged solution.

First of all the flow about the standard airfoil section NACA 0012 will be investigated within the incidence range

$$\alpha(T) = 13° + 5° \sin\omega^* T$$

and a Reynolds number of $2 \cdot 10^6$. In Ref. [15] a maximum lift coefficient of about $c_L = 1.55$ at $\alpha = 16°$ is achieved from experiments. In the present calculation a breakdown in the leading edge region due to the strong adverse pressure gradient occurred at $\alpha > 17°$.

Fig. 7 displays the boundary layer profiles (u-velocity component, Fig. 7a) and the corresponding streamlines obtained by integration of the u, v-velocity vector field on the upper surface of the airfoil in Fig. 7b. The coordinate s in Fig. 7 is the slope along the airfoil surface (measured from the trailing edge around the pressure side to the upper surface, see also Fig. 1). The coordinate η is measured normal to the surface and is restricted in Fig. 7 to a narrow region very close to the airfoil surface. The main features of these plots is the backflow region which has developed from the trailing edge upstream to about $s = 1.6$ ($x/c \approx 0.6$). This region extends outwards towards the trailing edge. It has been pointed out[4] that the backflow region is sensitively dependent on the location of transition for this very high incidence case. The transition point in the present calculation (steady as well as unsteady) was fixed two grid points ($\Delta x = 0.02$) downstream from the position of the stagnation point.

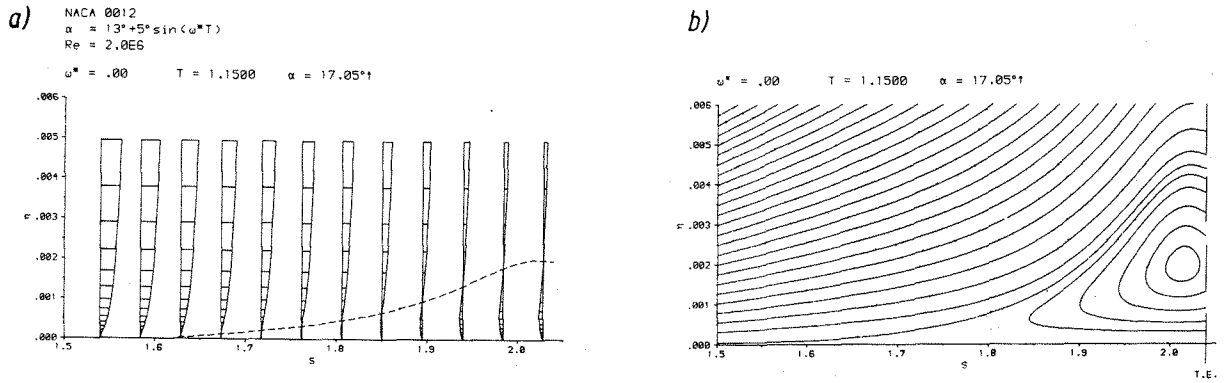

Figure 7: **Boundary layer details on NACA 0012 upper surface, steady incidence.**
a) *u*-velocity profiles b) streamlines

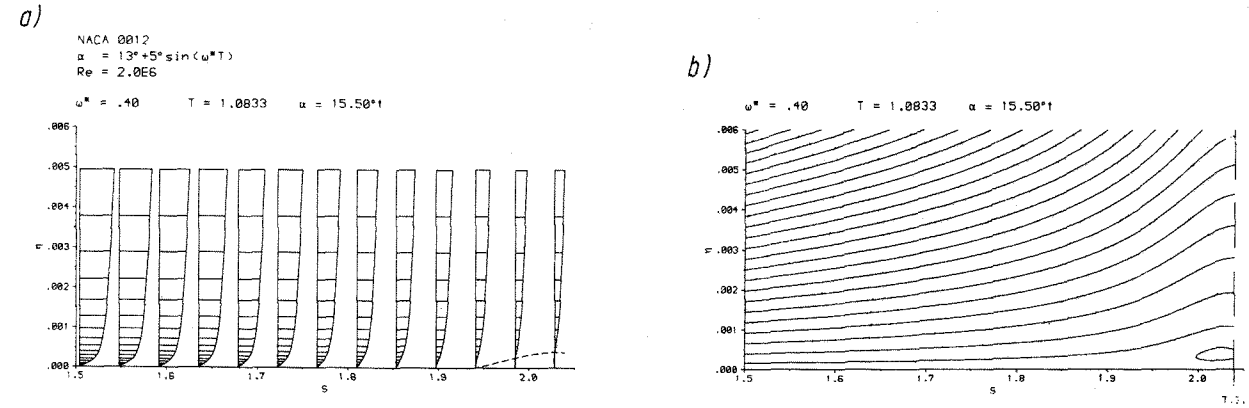

Figure 8: **Boundary layer details on NACA 0012 upper surface, oscillating case. Instantaneous incidence α = 15.5° upstroke**

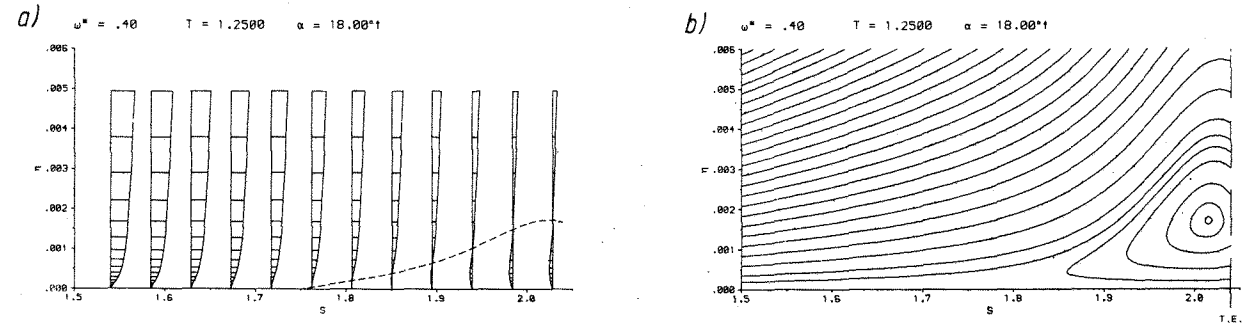

Figure 9: **Instantaneous incidence α = 18°**

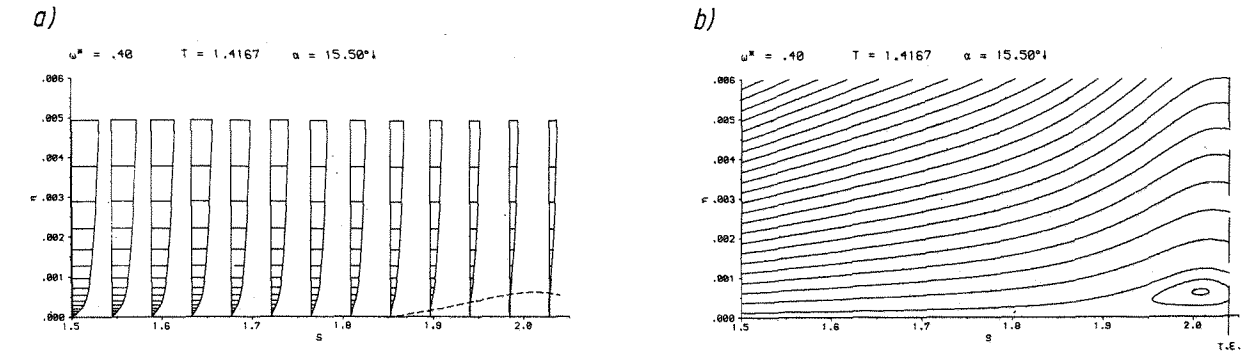

Figure 10: **Instantaneous incidence α = 15.5° downstroke**

Figs. 8, 9 and 10 show corresponding results from unsteady calculations with a reduced frequency of $\omega^* = 0.4$. Figs. 8 display the flow details at $\alpha = 15.5°$ upstroke, Figs. 9 include the results for the maximum incidence $\alpha = 18°$ and Figs. 10 show the results for $\alpha = 15.5°$ downstroke. Several features are noteworthy. First of all, the numerical calculation did not break down for the unsteady case. The region of backflow is smaller in its upstream extent ($\alpha = 18°$, Figs. 9) as well as in its extension in η-direction although the incidence with $\alpha = 18°$ is considerably higher as in the quasi-steady case (17°). If the frequency is increased further, the backflow region is reduced even more. Comparison between Figs. 8 and 10 ($\alpha = 15.5°\uparrow$ and $\alpha = 15.5°\downarrow$) show considerable phase shifts in the development and extent of the reversed flow regions.

Further details of the boundary layer development in space (s) and time ($\overline{T}$, Eq. 8) are displayed in ***Figs. 11 – 13*** for the three frequency cases $\omega^* = 0 / 0.4 / 0.8$ and the same airfoil incidence variation and Reynolds number as in Figs. 7 – 10. Figs. 11 show the development of the boundary layer displacement thicknesses δ^*, where in Fig. 11a (quasi-steady) irregularities occur in the trailing edge region for incidences beyond 17°. The calculations were forced to continue to larger incidences; the results in this region are therefore not assumed to be very meaningful. In the unsteady cases (Figs. 11b, 11c), however, the results do not show any numerical irregularities. This result is assumed to be of importance with respect to the increasing delay of breakdown of the unsteady lift with increasing frequency of oscillation. This is a phenomenon which has been frequently observed in experimental investigations as well. Comparing the three δ^* carpets (Figs. 11a, b and c) it is evident that a strong decrease of the displacement body occurs with increasing reduced frequency. It can be concluded from this behavior that, with increasing frequency, the influence of boundary layer displacement on the outer inviscid flow also decreases.

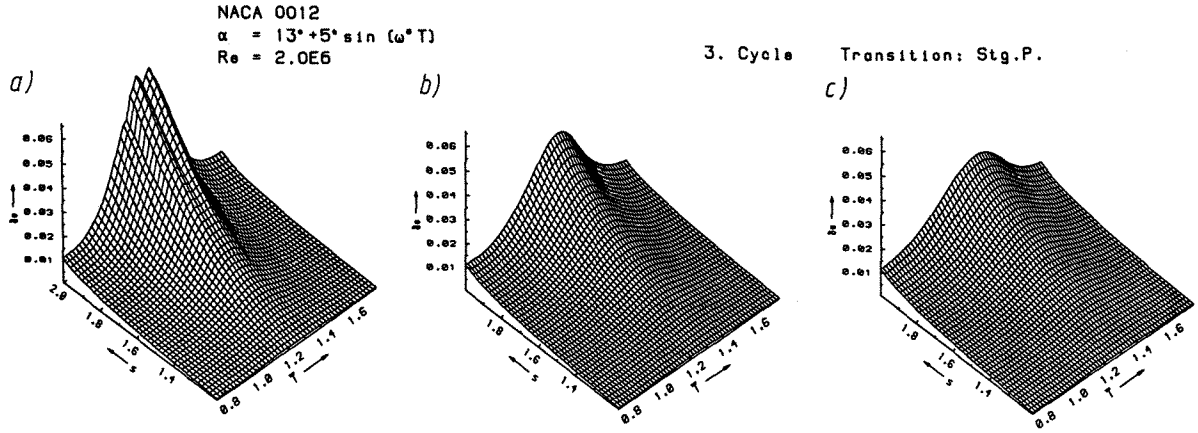

Figure 11: **Boundary layer displacement thickness δ^* in space/time domain.**
a) steady b) $\omega^* = 0.4$ c) $\omega^* = 0.8$

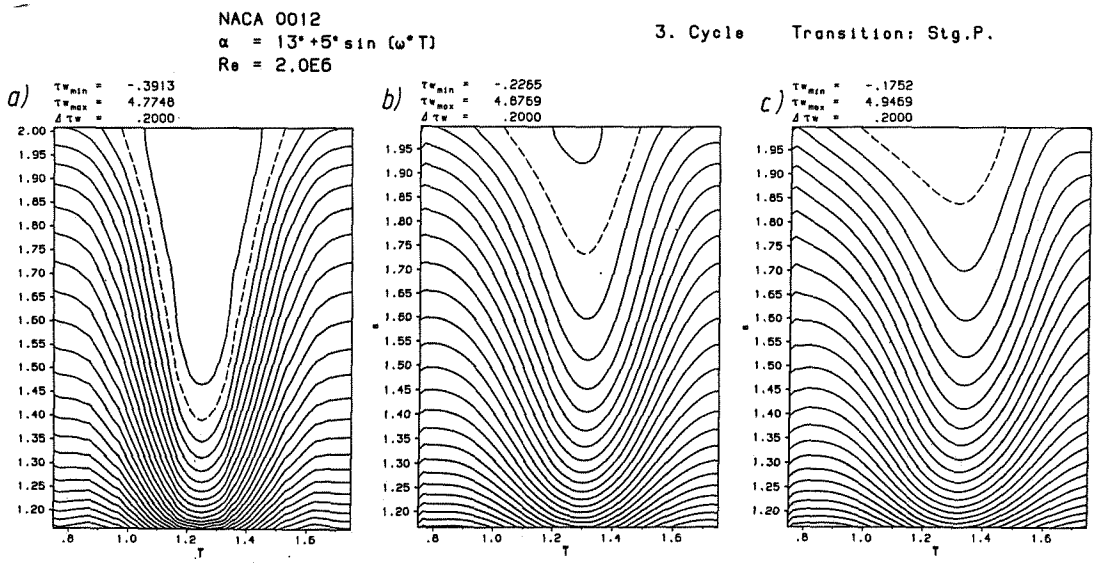

Figure 12: **Contour lines of wall shear stress τ_w in space/time domain.**
a) steady b) $\omega^* = 0.4$ c) $\omega^* = 0.8$

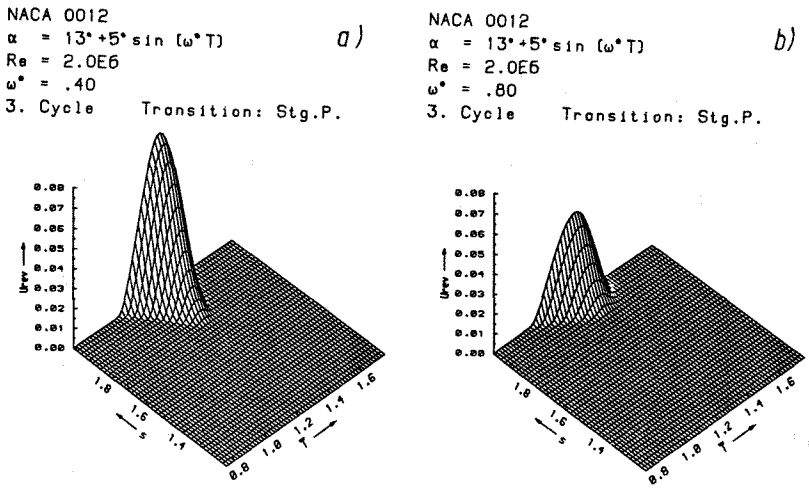

Figure 13: **Maximum reversed flow velocities within boundary layer.**
a) $\omega^* = 0.4$ b) $\omega^* = 0.8$

Figs. 12 display corresponding contour lines of the time-dependent wall shear stress

$$\tau_w = \frac{\partial u}{\partial \bar{\eta}}$$

again for the three ω^*-cases on the upper surface of the airfoil ($s = 2.03 \triangleq$ trailing edge, $\bar{T} = 1.0$ corresponds to $\alpha = 13°\uparrow$, $\bar{T} = 1.25 \triangleq \alpha = 18°$ and $\bar{T} = 1.5 \triangleq 13°\downarrow$). The dashed lines in these figures indicate the region of reversed flow. In Figs. 12b and 12c the locations of minimum wall shear are shifted to higher $\bar{T}$ values, i.e. into the downstroke region. The curves show increasing deformations.

Lastly, Figs. 13 display the maximum reversed flow velocities within the boundary layer. For $\omega^* = 0.4$ values about 8% of the freestream velocity are reached, decreasing to about 4.5% for the higher frequency ($\omega^* = 0.8$).

Figs. 14 and 15 display results which are important for the global coupling procedure. Figs. 14a and b show the development of $U\delta^*$ in space and time. Similar to plots 11, the maximum $U\delta^*$ values are reduced considerably with increasing frequency. The spatial derivative of ($U\delta^*$), Eq. (45), determines the blowing velocity v_B which is introduced into Eq. (46) to modify the kinematic flow condition in the inviscid code. Figs. 15a and b display contour lines of the blowing velocity for a complete cycle of oscillation. Noteworthy are the considerable phase shifts of the maximum v_B values to higher $\bar{T}$, i.e. into the downstroke region. It is of further interest that v_B has a maximum in the leading edge region within the area of strong velocity deceleration.

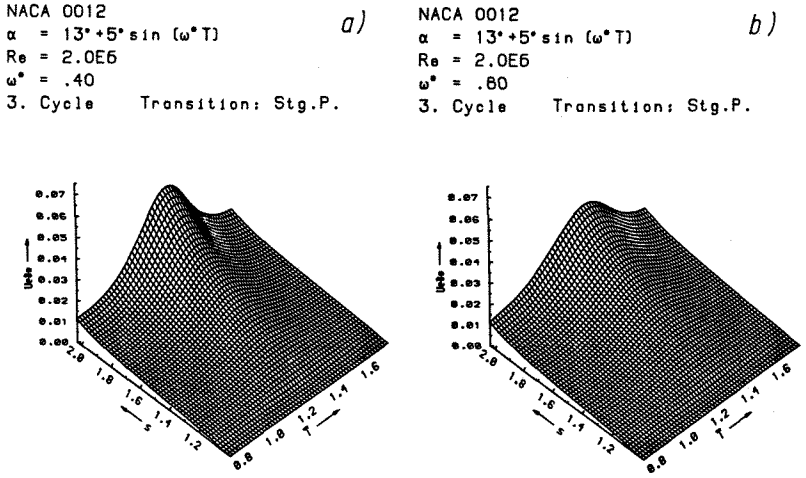

Figure 14: **$U_e\delta^*$ distributions in space/time domain.**
a) $\omega^* = 0.4$ b) $\omega^* = 0.8$

The latter phenomenon should be investigated in the future because it may force the formation of a strong interaction region with incipient turbulent leading edge separation.

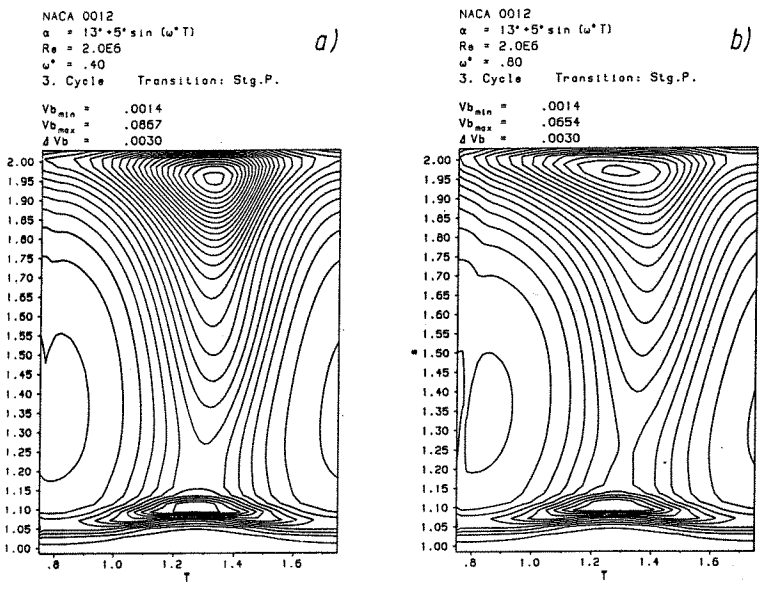

Figure 15: **Contour lines of blowing velocities v_B**
a) $\omega^* = 0.4$ b) $\omega^* = 0.8$

5.2 Lift, moment and drag distributions

Figs. 16a, b and c show the sectional lift and moment distributions on the NACA 0012 airfoil section for the three frequency cases. The solid curves in Figs. 16 display the inviscid results (after three inviscid cycles). The dashed curves show the results after three global cycles of viscous/inviscid interaction. Fig. 16a also includes experimental data from Abbott and v. Doenhoff.[15] In the experiment the maximum lift is obtained at about $\alpha = 16°$. The analytical results exceed this value. It has been mentioned in the previous section that a first breakdown of the boundary layer calculation occurred just beyond $\alpha = 17°$. In this region the lift curve shows noteworthy wiggles: the calculation was forced to continue here.

In the unsteady case, however, (Figs. 16b and c) the curves show a smooth behavior. As in the quasi-steady limit the lift is reduced throughout the entire cycle compared to the inviscid case. Increasing hysteresis effects can be observed with increasing reduced frequency.

Finally, ***Figs. 17, 18 and 19*** show results for three different airfoil sections: NACA 0012, Ames 01 and NLR 7301 with incidence variations, frequencies and Reynolds numbers which have been experimentally investigated.[2] The corresponding experimental data are indicated in the plots. These three cases were selected because the critical pressure on the airfoil leading edge was not exceeded and therefore compressibility effects should remain small. In all three cases the moment and drag distributions show good agreement with experimental data except for the c_M curve in Fig. 19 (NLR 7301) which is shifted in the experiment to higher negative values. The lift curves in all three cases however show a notable deviation. The experimental lift curves have a larger slope compared to the analytical results. There are not only deviations at higher incidence but also at the lowest α where viscous effects should be of only small importance. Furthermore the figures show that the measured maximum lift coefficients are even higher than the inviscid values. This is surprising because the inviscid values in these cases are reduced due to viscous effects. The explanation for these deviations may be that the amplitude of oscillation in the experimental case was higher than the nominal one: the curves should therefore be plotted over a larger incidence range which would reduce the slope of the curves accordingly.

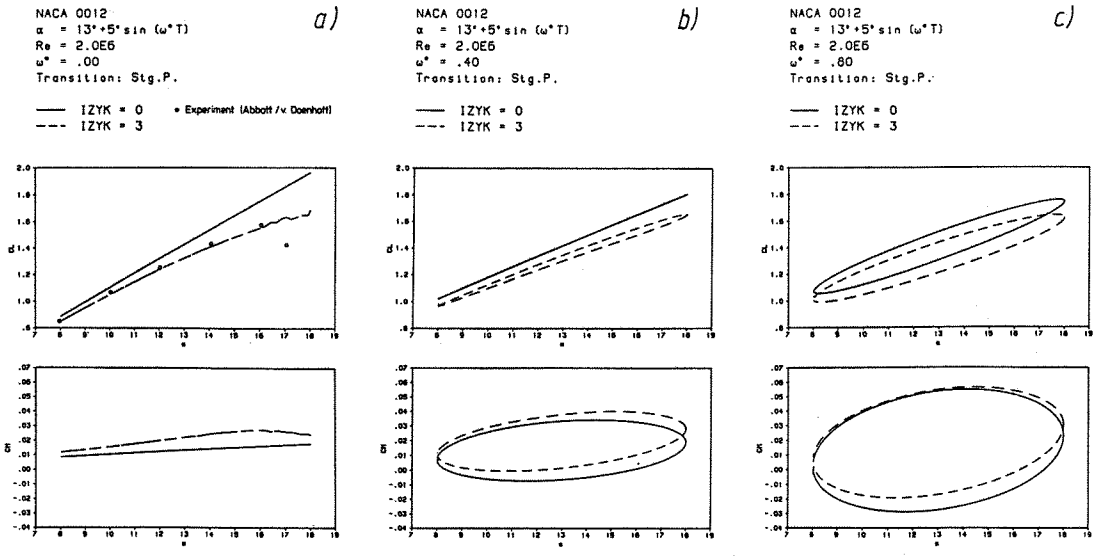

Figure 16: **Lift and moment distributions. a) steady, compared with experimental data[15] b) unsteady, $\omega^* = 0.4$ c) unsteady, $\omega^* = 0.8$**

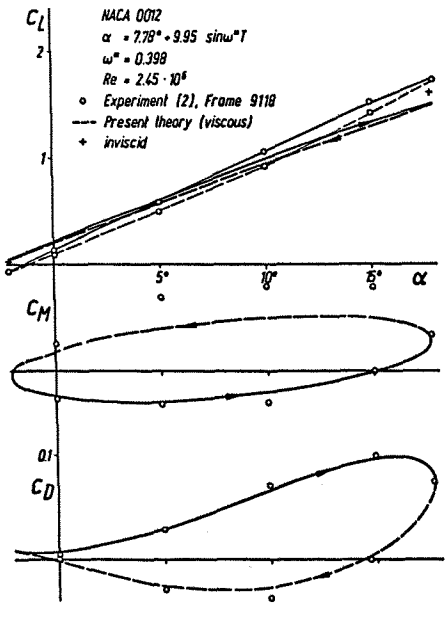

Figure 17: **Lift, drag and moment distributions, comparison with experimental data;[2] NACA 0012**

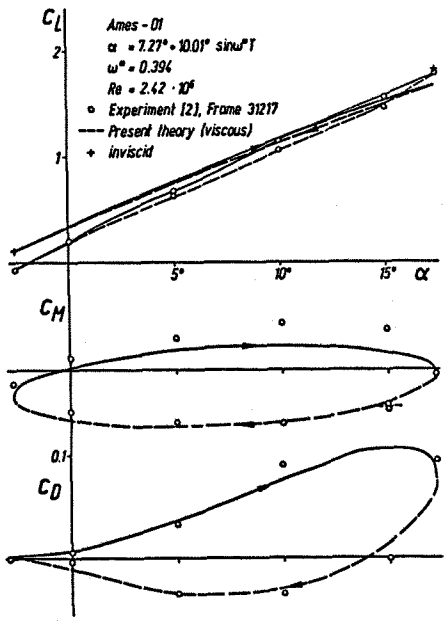

Figure 18: **Lift, drag and moment distributions, comparison with experimental data;[2] AMES 01**

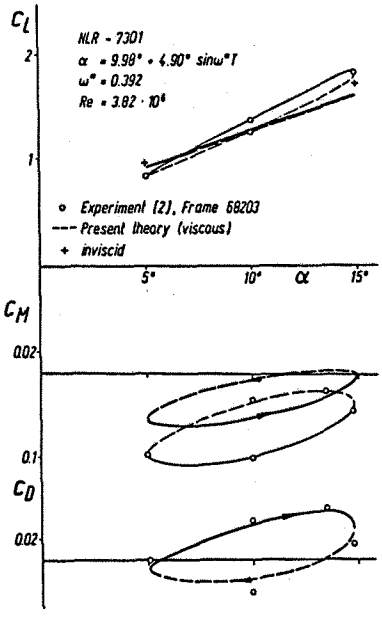

Figure 19: **Lift, drag and moment distributions, comparison with experimental data;[2] NLR 7301**

6. Conclusion

For calculation of unsteady airloads on oscillating airfoils in the high incidence regime, a coupling procedure between an inviscid potential theoretical panel method and an unsteady interactive boundary layer calculation procedure has been developed. A coordinate transformation into a time-dependent surface coordinate has been incorporated into the boundary layer code: the surface coordinate is attached to the moving stagnation point as well as to the airfoil trailing edge. With this transformation a quasi-steady treatment of the viscous flow equations in the leading edge region is avoided. The upper and lower sides of the airfoil are calculated with the complete set of unsteady equations. Moreover it is straightforward to extend the interactive region of the boundary layer calculation over the complete upper surface of the airfoil while accounting for interaction areas in the region of strong adverse pressure gradients with incipient separation.

The method has been applied for a number of incidence cases up to $\alpha(T) \approx 18°$, reduced frequencies, including the quasi-steady case, Reynolds numbers and various airfoil sections. The comparisons with experimental data show reasonably good agreement even for the unsteady drag coefficients.

The method nevertheless has several shortcomings. The incompressible treatment reaches its limits in high-incidence cases due to the development of supersonic regions and shock waves in the leading edge area of the airfoil. The displacement effect of the wake has been represented simply by an analytical formula. The unsteady movement of transition has been rigidly attached to the increment of the stagnation point. The turbulence model is applied on a quasi-steady basis. Future plans foresee avoiding at least some of these shortcomings by a further development of the coupling procedure.

Bibliography

[1] Liiva, J., Davenport, F.J., Gray, L., Walles, I.C. *Two-Dimensional Test of Airfoils Oscillating Near Stall.* USA AVLABS TR 68-13A/B (1968).

[2] McCroskey, W.J., McAlister, K.W., Carr, L.W., Pucci, S.L. *An Experimental Study of Dynamic Stall on Advanced Airfoil Sections.* NASA TM 84245 (1984); also: USA AVRADCOM TR 82-A-8 (1982).

[3] Geißler, W., Carr, L.W., Cebeci, T. *Unsteady Separation Characteristics of Airfoils Operating under Dynamic Stall Conditions.* Paper No. 32, 12th European Rotorcraft Forum, Sept. 22 – 25, 1986, Garmisch-Partenkirchen, W. Germany.

[4] Cebeci, T., Cark, R.W., Chang, K.C., Halsey, N.D., Lee, K. *Airfoils with Separation and the Resulting Wakes.* J. Fluid Mechanics Vol. 163 (1986) pp. 323 – 347.

[5] Barnett, M., Verdon, J.M. *Viscid/Inviscid Interaction Analysis of Subsonic Turbulent Trailing-Edge Flows.* AIAA Journal Vol. 25, No. 9 (1987) pp. 1184 – 1193.

[6] Bradshaw, P., Cebeci, T., Whitelaw, J.H. *Engineering Calculation Methods for Turbulent Flow.* Academic Press, 1981.

[7] Geißler, W. *Calculation of Unsteady Airloads on Oscillating Profiles by y Time-Marching Procedure.* DFVLR Internal Report 232 – 84 J 05 (1984).

[8] Geißler, W. *Unsteady Laminar Boundary-Layer Calculations on Oscillating Configurations Including Backflow. Part II: Airfoil in High-Amplitude Pitching Motion – Dynamic Stall.* NASA TM 84319, Juli 1983.

[9] Cebeci, T., Khuttab, A.A., Schimke, S.M. *Separation and Reattachment near the Leading Edge of an Oscillating Airfoil.* J. Fluid Mechanics Vol. 180 (1988) pp. 253 – 274.

[10] Cebeci, T., Smith, A.M.O. *Analysis of Turbulent Boundary Layers.* New York: Academic Press, 1974.

[11] Veldman, A.E.P. *New Quasi-Simultaneous Method to Calculate Interacting Boundary Layers.* AIAA Journal Vol. 19 (1981) p. 769.

[12] Keller, H.B. *Accurate Finite Difference Methods for Two-Point Boundary Value Problems.* SIAM Journal of Numerical Analyses, 11 (1974) p. 305.

[13] Cebeci, T., Bradshaw, P. *Momentum Transfer in Boundary Layers.* Washington: Hemisphere – McGraw-Hill, (1977).

[14] Schlichting, H., Truckenbrodt, E. *Aerodynamik des Flugzeuges.* Band 2. Berlin, Göttingen, Heidelberg: Springer, 1960.

[15] Abbott, J.H., von Doenhoff, A.E. *Theory of Wing Sections.* Dover, 1959.

Appendix

With the abbreviations

$$FB = 0.5\,(\bar{\psi}_{j,2,2} + \bar{\psi}_{j-1,2,2})$$

and correspondingly

$$UB(u),\ VB(g),\ WB(W)$$

$$\begin{aligned} FB2 &= 0.5\,(\bar{\psi}_{j,2,1} + \bar{\psi}_{j-1,2,1}) \\ FB3 &= 0.5\,(\bar{\psi}_{j,1,1} + \bar{\psi}_{j-1,1,1}) \\ FB4 &= 0.5\,(\bar{\psi}_{j,1,2} + \bar{\psi}_{j-1,1,2}) \end{aligned} \tag{A1}$$

and correspondingly

$$UB2,\ UB3,\ UB4 \quad \text{and} \quad WB2,\ WB3,\ WB4$$

$$\begin{aligned} FB14 &= 0.5\,(FB + FB4) \\ FB23 &= 0.5\,(FB2 + FB3) \end{aligned}$$

and correspondingly

$$UB14,\ UB23,\ WB14,\ WB23,$$
$$UB12,\ UB34,\ WB12,\ WB34$$

$$\begin{aligned} UB1234 = 0.5\,(&u_{j,2,2}+u_{j-1,2,2}+u_{j,2,1}+ \\ &u_{j-1,2,1}+u_{j,1,2}+u_{j-1,1,2}+u_{j,1,1}+u_{j-1,1,1}) \end{aligned}$$

and correspondingly

$$VB1234,\ WB1234,\ UB1234$$

$$\begin{aligned} UBSQ12 &= 0.25\,(u^2_{j,2,2} + u^2_{j-1,2,2} + u^2_{j,2,1} + u^2_{j-1,2,1}) \\ UBSQ34 &= 0.25\,(u^2_{j,1,1} + u^2_{j-1,1,1} + u^2_{j,1,2} + u^2_{j-1,1,2}) \end{aligned}$$

and correspondingly

$$WBSQ12,\ WBSQ34.$$

With these abbreviations, the right-hand terms of Eqs. (17) – (20) and (32) yield

$$(r_1)_j = \bar{\psi}_{j-1,2,2} + \bar{\psi}_{j,2,2} + h_{j-1}\,UB\ , \tag{A2}$$

(A3)

$$\begin{aligned} (r_2)_j = &\frac{4}{\Delta\tau}\,(UB14 - UB23) - \frac{4}{\Delta\tau}\,(WB14 - WB23) + \\ &+ \frac{2}{\Delta\xi}\left(\frac{\partial\xi}{\partial x}\right)(UBSQ12 - UBSQ34) - \\ &- \frac{2}{\Delta\xi}\left(\frac{\partial\xi}{\partial x}\right)(WBSQ12 - WBSQ34) + \\ &+ \frac{4\,DKSI}{\Delta\xi}\,(UB12 - UB34) - \frac{4\,DKSI}{\Delta\xi}\,(WB12 - WB34) + \\ &+ \frac{DDKSI}{\Delta\xi}\,UB1234 - \frac{DDKSI}{\Delta\xi}\,WB1234 - \\ &- \frac{1}{\Delta\xi}\,VB1234\,(FB12 - FB34) - \\ &- \frac{1}{\Delta\eta_{j\ 1}}\,\{(b\cdot g)_{j,2,2} - (b\cdot g)_{j\ 1,2,2} + (b\cdot g)_{j,2,1} - (b\cdot g)_{j\ 1,2,1} + \\ &+ (b\cdot g)_{j,1,2} - (b\cdot g)_{j-1,1,2} + (b\cdot g)_{j,1,1} - (b\cdot g)_{j\ 1,1,1}\} \end{aligned}$$

with the metric coefficients

$$DKSI = 0.25\left\{\left(\frac{\partial\xi}{\partial t}\right)_{1,1} + \left(\frac{\partial\xi}{\partial t}\right)_{1,2} + \left(\frac{\partial\xi}{\partial t}\right)_{2,1} + \left(\frac{\partial\xi}{\partial t}\right)_{2,2}\right\}$$

and

$$DDKSI = \left\{0.5\left[\left(\frac{\partial\xi}{\partial t}\right)_{2,2} + \left(\frac{\partial\xi}{\partial t}\right)_{2,1}\right] - 0.5\left[\left(\frac{\partial\xi}{\partial t}\right)_{1,1} + \left(\frac{\partial\xi}{\partial t}\right)_{1,2}\right]\right\}.$$

$$\begin{aligned} (r_3)_{j-1} &= u_{j-1,2,2} + u_{j,2,2} + h_j\,VB \\ (r_4)_{j-1} &= W_{j-1} - W_j\ . \end{aligned} \tag{A4}$$

The coefficients from the linearized momentum equation (17) yield

(A5)

$$\begin{aligned} (S1)_j &= \frac{1}{2\Delta\xi}\,(FB12 - FB34) + \frac{1}{\Delta\eta_{j-1}}\,b_{j,2,2} \\ (S2)_j &= \frac{1}{2\Delta\xi}\,(FB12 - FB34) - \frac{1}{\Delta\eta_{j-1}}\,b_{j-1,2,2} \\ (S3)_j &= \frac{1}{4\Delta\xi}\,VB1234 \equiv (S4)_j \\ (S5)_j &= -\frac{1}{\Delta\tau} - \frac{u_{j,2,2}}{\Delta\xi}\left(\frac{\partial\xi}{\partial x}\right) - \frac{DKSI}{\Delta\xi} - \frac{DDKSI}{2\Delta\xi} \\ (S6)_j &= -\frac{1}{\Delta\tau} - \frac{u_{j-1,2,2}}{\Delta\xi}\left(\frac{\partial\xi}{\partial x}\right) - \frac{DKSI}{\Delta\xi} - \frac{DDKSI}{2\Delta\xi} \\ (S7)_j &= \frac{1}{\Delta\tau} + \frac{W_{j,2,2}}{\Delta\xi}\left(\frac{\partial\xi}{\partial x}\right) + \frac{DKSI}{\Delta\xi} + \frac{DDKSI}{2\Delta\xi} \\ (S8)_j &= \frac{1}{\Delta\tau} + \frac{W_{j-1,2,2}}{\Delta\xi}\left(\frac{\partial\xi}{\partial x}\right) + \frac{DKSI}{\Delta\xi} + \frac{DDKSI}{2\Delta\xi}\ . \end{aligned}$$

The underlined terms in Eqs. (A3) and (A5) are also obtained by transforming the system (17) – (20) and (32) into a moving coordinate system.